Available online at www.sciencedirect.com
ScienceDirect
Trans. Nonferrous Met. Soc. China 33(2023) 1963−1976
Transactions of Nonferrous Metals Society of China
www.tnmsc.cn

Effect of Cu content on intergranular corrosion and exfoliation corrosion susceptibility of Al−Zn−Mg−(Cu) alloys

Meng-han ZHANG[1,2], Sheng-dan LIU[1,2,3], Jing-yu JIANG[4], Wei-chang WEI[1,2]

1. School of Materials Science and Engineering, Central South University, Changsha 410083, China;
2. Key Laboratory of Non-ferrous Metals Science and Engineering, Ministry of Education, Central South University, Changsha 410083, China;
3. National Key Laboratory of Light and High Strength Structural Materials, Central South University, Changsha 410083, China;
4. School of Metallurgy and Environment, Central South University, Changsha 410083, China

Received 9 February 2022; accepted 11 May 2022

Abstract: The effect of Cu content on intergranular corrosion (IGC) and exfoliation corrosion (EXCO) susceptibility of Al−Zn−Mg−(Cu) alloys was investigated by electrochemical test, immersion test, electron backscattered diffraction, optical microscope, scanning electron microscope, scanning transmission electron microscope and scanning Kelvin probe force microscope. As Cu content increases from 0 to 2.6 wt.%, IGC susceptibility increases, while EXCO susceptibility first increases and then decreases, reaching the maximum at Cu content of 1 wt.%. With the increase of Cu content, the area fraction of recrystallized grains increases, and the aspect ratio of recrystallized grains first decreases and then increases; moreover, the Volta potential difference between grain boundary precipitates (GBPs) and the matrix increases, making GBPs more susceptible to corrosion. The initiation and propagation of IGC and EXCO are discussed mainly based on the features of GBPs, grain structure, and the Volta potential difference between GBPs and the matrix.

Key words: copper; intergranular corrosion; exfoliation corrosion; Al−Zn−Mg−Cu alloy; scanning Kelvin probe force microscope

1 Introduction

Al−Zn−Mg−Cu alloys have high specific strength and good plasticity, and are widely used in aerospace and transportation fields [1,2]. These alloys are typical age-hardenable alloys. After aging, a large amount of fine and dispersed η' strengthening phases form in the matrix, and significantly improve the strength [3,4]; but at the same time, grain boundaries (GBs) are covered by η phase ($MgZn_2$) [5]. The corrosion potential of η phase is lower than that of the matrix [6−8], so that it is attacked preferentially in corrosive solution. As a result, these alloys are susceptible to localized corrosion that generally propagates along GBs, such as intergranular corrosion (IGC) and exfoliation corrosion (EXCO). The occurrence of localized corrosion can lead to premature fracture and failure of alloys, bringing about huge risks [9,10]. Chemical composition, quenching and aging can significantly affect the features of grain boundary precipitates (GBPs) and precipitate-free zone (PFZ), and therefore affect the IGC and EXCO susceptibility [11−15].

Among the main alloying elements, Cu can promote the nucleation of GP zones and η' phase, and then can effectively improve the strength of Al−Zn−Mg−Cu alloys [16]. However, Cu exerts complicated effects on the corrosion susceptibility.

Corresponding author: Sheng-dan LIU, Tel: +86-731-88830265, E-mail: lsd_csu@csu.edu.cn
DOI: 10.1016/S1003-6326(23)66236-3

Some investigations showed that Cu can increase the corrosion potential of the matrix [17,18]; the higher Cu content in η phase at GBs makes it more noble, which can reduce the rate of dissolution of η phase and thus a lower rate of corrosion propagation [19−23]. This is beneficial to high resistance to IGC and EXCO. MARLAUD et al [12] showed that compared with 7449 alloy (1.9 wt.% Cu) and PA alloy (1.6 wt.% Cu), EXCO susceptibility of 7150 alloy (2.2 wt.% Cu) is lower; in 7150 alloy, the Cu enrichment in GBPs decreases the local corrosion driving force. LI et al [24] found that as Cu content increases from 0.8 to 2.2 wt.% in Al−8.54Zn−2.41Mg−*X*Cu alloys, the susceptibility of both IGC and EXCO first decreases and then increases, reaching the lowest at *X*=1.3 wt.%. It was thought that increasing Cu content can decrease the corrosion potential difference between GBPs and the matrix, but no experimental data were given; while excessively high Cu content results in a large amount of residual phase, which is not conducive to corrosion resistance. However, some investigations showed that the addition of Cu increases IGC and EXCO susceptibility [25−27]. YUAN et al [25] reported that as Cu content increases from 0.9 to 2.26 wt.% in Al−9.0Zn−2.0Mg−*X*Cu alloys, IGC and EXCO susceptibility increases; it was thought that corrosion initiation is easier to occur in alloys with higher Cu content, but the reason is not clear. DONG et al [26] found that with Cu content increasing from 0.8 to 2.2 wt.% in Al−9.3Zn−2.4Mg−*X*Cu alloys, IGC susceptibility increases, while EXCO susceptibility first decreases and then increases, and EXCO resistance is the highest at the Cu content of 1.5 wt.%; the mechanism was not well understood.

In this work, the effect of Cu content (0−2.6 wt.%) on IGC and EXCO susceptibility was investigated. Based on the features of GBPs, grain structure, and the Volta potential difference between GBPs and the matrix, the mechanism was explored. It can help to have better understanding of the effect of Cu on localized corrosion behavior of Al−Zn−Mg−(Cu) alloys.

2 Experimental

2.1 Materials

Three hot-rolled Al−Zn−Mg−Cu alloy sheets with a thickness of 3.5 mm were used in this work, and their chemical compositions are given in Table 1. Samples with a length of 60 mm in the rolling direction (RD), a width of 178 mm in the transverse direction (TD) were prepared. After solution heat treatment at 450 °C for 1 h and then 473 °C for 0.5 h in an air furnace, the samples were quenched in room temperature water, and then, artificially aged at 120 °C for 24 h in the oil bath.

Table 1 Chemical composition of investigated alloys (wt.%)

Alloy	Zn	Mg	Cu	Zr	Si	Fe	Al
0Cu	9.04	1.41	−	0.12	0.022	0.087	Bal.
1Cu	9.08	1.51	1.01	0.13	0.021	0.078	Bal.
2.6Cu	8.83	1.49	2.68	0.12	0.020	0.084	Bal.

2.2 Accelerated immersion tests

Samples with a length of 20 mm in RD and a width of 30 mm in TD were prepared for IGC tests according to GB/T 7998—2005 specification [28]. The RD−TD surfaces were ground to 1500 grit by abrasive papers and then polished by 0.5 μm diamond pastes. Subsequently, after immersion in NaOH solution for 10 min, samples were washed with water and then immersed in HNO_3 solution until the surfaces were bright. Samples were immersed in a solution containing 1 mol/L NaCl and 0.1 mol/L H_2O_2, and the temperature was maintained at (35±2) °C in a water bath. After immersion for 10 min, the corrosion morphology of samples was observed by ZEISS EVO MA10 scanning electron microscope (SEM) with an Oxford X-Max^N energy dispersive X-ray spectroscope (EDS). To investigate the development of IGC, some samples were immersed in IGC solution for 0.5, 2, 6, 12, 24 and 48 h, respectively; metallographic samples were cut and prepared to measure the maximum corrosion depth, which was performed using Leica DM2700M optical microscope (OM).

EXCO tests were performed in an aqueous solution of 4.0 mol/L NaCl, 0.5 mol/L KNO_3 and 0.1 mol/L HNO_3 at (25±3) °C in a water bath according to GB/T 22639—2008 specification [29]. The RD−TD section was exposed with an area of 6 cm^2, and the ratio of solution volume to exposed surface area was 20 mL/cm^2. Similarly, the surface morphology of the sample was observed by SEM after immersion for 10 min; Seven samples were prepared and immersed in EXCO solution for 0.5,

1, 2, 6, 12, 24, and 48 h, respectively, to observe corrosion morphology and measure the corrosion depth by OM. Based on the visual examination and metallographic examination, the EXCO rating can be evaluated to be pitting (P), superficial exfoliation (EA), moderate exfoliation (EB), severe exfoliation (EC), or very severe exfoliation (ED).

2.3 Electrochemical tests

The polarization curves were measured using AUTOLAB M204 instrument with a platinum counter electrode, a silver/silver chloride reference electrode and a working electrode. The RD−TD surface was exposed with an area of 1 cm^2, and the other surfaces were protected by resin. To ensure reliable results, six samples of each alloy were prepared and tested. The polarization curve measurements were performed at room temperature in EXCO solution and IGC solution, respectively.

2.4 Microstructure examination

Samples were electrolytically polished in a solution of 10% perchloric acid with 90% ethanol, and then examined using a JSM−7900F SEM with an OXFORD electron backscattered diffraction (EBSD) detector to investigate grain structure. Samples were carefully ground to be about 80 μm and punched into discs with a diameter of 3 mm, and then thinned by electropolishing in a solution of 80% methanol and 20% nitric acid below −25 °C in liquid nitrogen. Subsequently, some GBPs of samples were examined by Titan G^2 60−300 scanning transmission electron microscope (STEM) equipped with a high angle annular dark field (HAADF) detector and a Super-X EDS detector, and the beam spot size was 1 nm and operating voltage was 300 kV.

2.5 Surface Volta potential measurement

Samples with a length of 10 mm in RD and a width of 5 mm in TD were prepared for the surface Volta potential measurement. After polishing, some indentations were made by Wilson VH1202 Vickers Hardness tester to mark the GBs in samples. Then, the surface was measured at a scanning rate of 0.5 Hz using a Bruker Dimension FastScan atomic force microscope equipped with a CoCr layered silicon electrode as the reference electrode. After test, the samples were etched with Graff reagent (1 mL HF, 16 mL HNO_3, 3 g CrO_3 and 83 mL H_2O) to show grain structure and examined by OM.

3 Results

3.1 Microstructure

3.1.1 Grain structure

Figure 1 shows EBSD orientation maps of samples with different Cu contents. The low angle GBs (2°−15°) indicated by white lines are regarded as subgrain boundaries (SGBs), and the high angle GBs (>15°) are indicated by black lines. These samples show a partially-recrystallized microstructure, which is a typical grain structure of hot-rolled Al−Zn−Mg−Cu alloys after solution heat

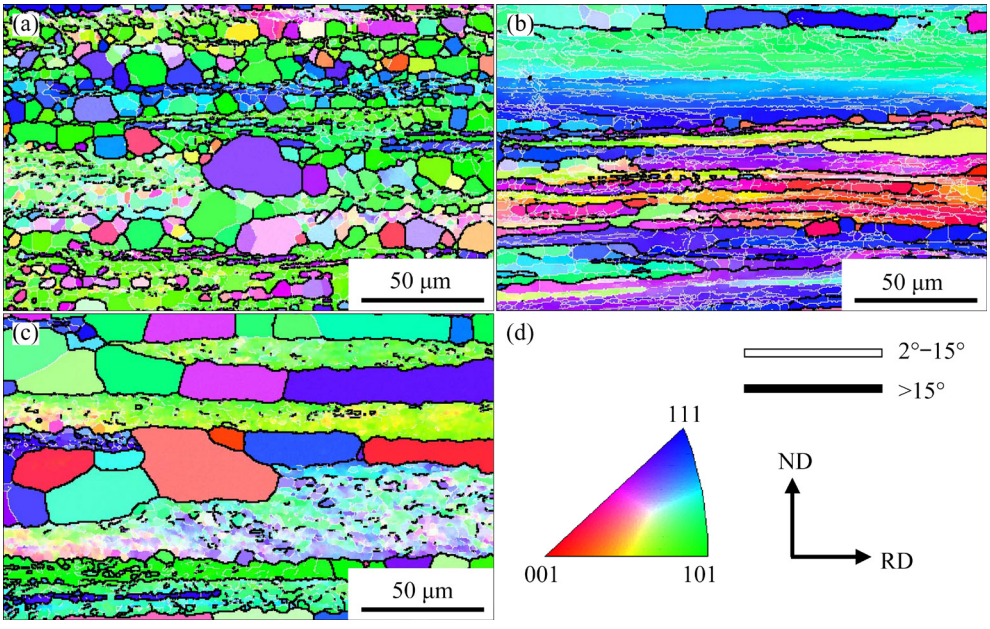

Fig. 1 Typical orientation maps of samples: (a) 0Cu; (b) 1Cu; (c) 2.6Cu; (d) Crystallographic feature

treatment [30]. With the increase of Cu content, the size and the area fraction of recrystallized grains gradually increase. In 0Cu and 2.6Cu samples, the recrystallized grains tend to be elongated along the RD and distributed in layers along the ND, as shown in Figs. 1(a, c); while in 1Cu sample, most recrystallized grains are small and exhibit equiaxed-shape, as shown in Fig. 1(b).

The recrystallization behavior of hot-deformed Al−Zn−Mg−Cu alloys during solution treatment is very complicated and it is believed that particle stimulated nucleation is the main recrystallization mechanism [31], but in situ recrystallization and recrystallization by strain induced boundary migration can also occur [32]. Recrystallization is related to the second phase and deformation energy storage of samples after hot deformation [31,32]; different Cu contents may cause the changes in these factors, and then results in a very complex recrystallization mechanism.

Based on EBSD images, the quantitative results of the grain structure features are summarized in Table 2. With the increase of Cu content, the length ratio of SGBs decreases, while the length ratio of GBs first increases and then decreases, and it is the largest in 1Cu sample. Moreover, the length along RD of recrystallized grains first decreases and then increases with a slight increase in the length along ND. As a result, the average aspect ratio is the smallest, about 1.8 in 1Cu sample.

3.1.2 Precipitates at grain boundaries

IGC and EXCO generally propagate along GBs [33]. HAADF-STEM images of precipitates at GBs for different samples are shown in Fig. 2. There are fine and dispersed η' strengthening phases in the interior of grains, and bright and rod-like η phases are located at GBs. Due to the anodic nature [6−8], some η phase particles are etched out during TEM sample preparation, and consequently some black holes at GBs can be seen. For the three samples, GBPs are closely-spaced with a length of 10−50 nm and a width of 5−15 nm, and the width of PFZs is similar, approximately 20 nm. Based on EDS measurements, the chemical compositions of GBPs are given in Fig. 3. In all the samples, the ratio of Zn content to Mg content in GBPs is about 2:1. As Cu content increases from 0 to 2.6 wt.%, there is a slight difference in the content of Zn and Mg in GBPs, while the content of Cu in GBPs increases from 0 to 9.0 at.%. As Cu content in the alloy increases, more Cu atoms can segregate at GBs, and as a result, GBPs with higher Cu content are formed at GBs [34,35].

Table 2 Grain structure features based on EBSD images of different samples

Feature of grain structure	0Cu	1Cu	2.6Cu
Recrystallization fraction/%	17.3±2.8	37.4±4.0	62.8±4.7
Length ratio of GBs/mm^{-1}	118.9±29.7	253.6±26.1	129.9±27.4
Length ratio of SGBs/mm^{-1}	535.7±42.3	206.1±25.6	124.6±19.2
Length along RD of recrystallized grains/μm	106.2±48.6	19.4±4.9	46.2±20.2
Length along ND of recrystallized grains/μm	8.7±2.1	10.1±3.7	12.8±5.8
Aspect ratio of recrystallized grains	12.2±6.1	1.8±0.9	4.1±1.7

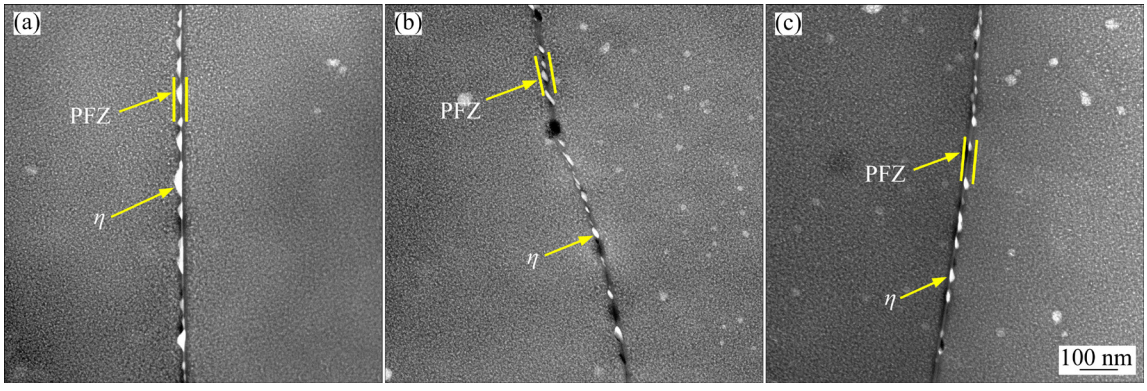

Fig. 2 HAADF-STEM images showing precipitates at GBs of samples: (a) 0Cu; (b) 1Cu; (c) 2.6Cu

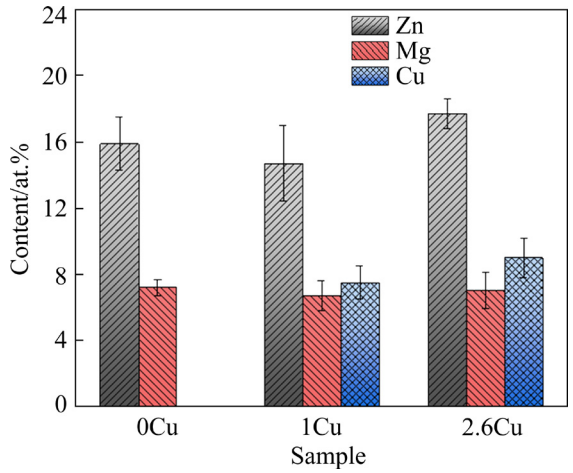

Fig. 3 Chemical compositions of GBPs in samples

3.2 Immersion results in IGC solution

Typical SEM images of samples before and after immersion in IGC solution for 3 and 10 min are shown in Fig. 4. Before immersion, some bright and coarse particles with a size of several microns can be observed, as shown in Figs. 4(a_1, b_1, c_1). The EDS test results show that for 0Cu sample, these particles primarily contain (85.6±3.0) at.% Al, (11.1±4.0) at.% Fe, (2.4±0.9) at.% Zn and (0.9±0.3) at.% Mg, and they are likely Al_3Fe phases [36]. For 1Cu sample, these particles mainly contain (81.2±2.4) at.% Al, (11.7±1.5) at.% Fe, (3.1±0.3) at.% Cu, (2.7±0.4) at.% Zn, and (1.3±0.2) at.% Mg, and they are likely $Al_{23}Fe_4Cu$ phases [37,38]. For 2.6Cu sample, these particles mainly contain (70.6±4.5) at.% Al, (9.3±1.6) at.% Fe, (18.9±3.7) at.% Cu, (0.8±0.1) at.% Zn, and (0.4±0.1) at.% Mg, and they are likely Al_7Cu_2Fe phases [39]. These phases are cathodic with respect to the matrix [8,39,40]. After immersion for 3 min, the surrounding matrix of Fe-containing particles of the three samples is corroded, leading to tiny pits, as shown by the arrows in Figs. 4(a_2, b_2, c_2). After immersion for 10 min, larger pits are visible around Fe-containing particles in these samples, as shown by the solid arrows in Figs. 4(a_3, b_3, c_3). However, for 1Cu and 2.6Cu samples, there are some pits in the matrix away from Fe-containing particles, as shown by the dotted arrows in Figs. 4(b_3, c_3), and the number is larger in the latter sample. This is likely because of the corrosion of η phase at GBs.

After the immersion for 48 h, the surface morphology is shown in Fig. 5. In 0Cu sample, there are some black pits on the surface, as shown in Fig. 5(a). From Fig. 5(b), in 1Cu sample, in addition to pits, there are some cracks distributed

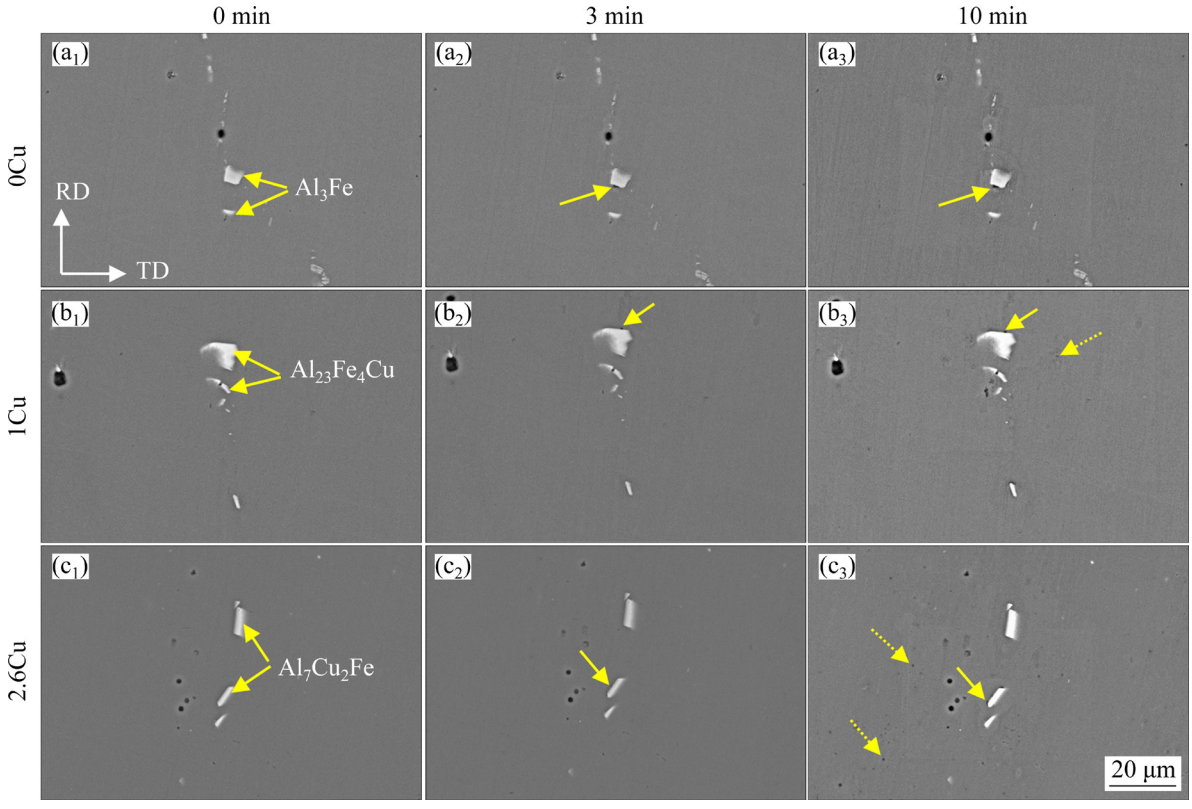

Fig. 4 SEM images of samples before and after immersion in IGC solution for different time

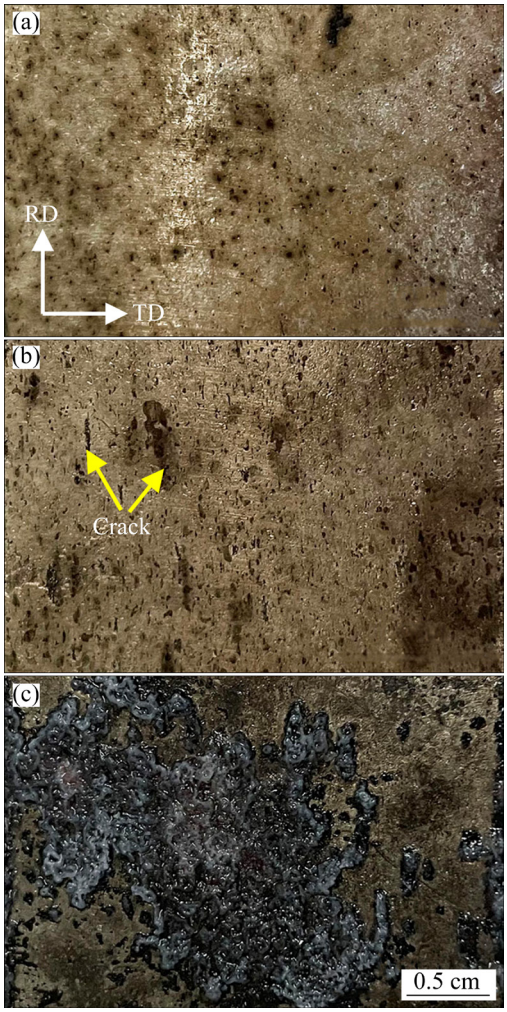

Fig. 5 Digital images showing surface morphology of samples after immersion in IGC solution for 48 h: (a) 0Cu; (b) 1Cu; (c) 2.6Cu

along the RD on the surface. For 2.6Cu sample, the surface is corroded severely, and a lot of corrosion products can be observed, as shown in Fig. 5(c). With the increase of Cu content, IGC tends to be more serious.

In order to further understand the IGC behavior, the cross section of the samples was examined by OM after immersion for different time. As an example, optical micrographs of samples after immersion for 48 h are shown in Fig. 6. From Fig. 6(a), in 0Cu sample, there are only some corrosion pits after immersion in IGC solution for 48 h. In 1Cu sample, there are mainly corrosion pits, and the corrosion propagation along GBs is occasionally observed, as shown in Fig. 6(b). For 2.6Cu sample, the corrosion tends to propagate along GBs, and IGC is clearly visible, as shown in Fig. 6(c).

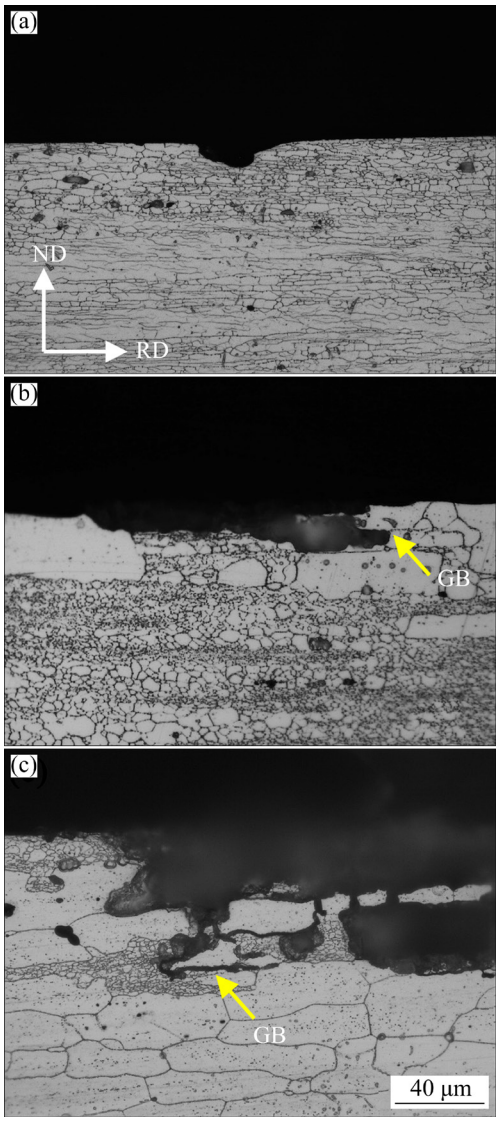

Fig. 6 Optical micrographs of cross section of samples after immersion in IGC solution for 48 h: (a) 0Cu; (b) 1Cu; (c) 2.6Cu (The cross section of samples was etched with Graff reagent)

In addition, the maximum corrosion depth of samples was measured after immersion for different time, as shown in Fig. 7. For 0Cu sample, only pitting occurs during immersion, and the pit depth slightly increases with the increase of immersion time. For 1Cu sample, there is pitting after immersion up to 2 h; after 2 h, corrosion propagation along GBs can be occasionally observed, and the depth of IGC rapidly increases with the increase of immersion time. For 2.6Cu sample, IGC can be observed after immersion for 0.5 h and the corrosion depth is about 31 μm. Then, as immersion time increases, the corrosion depth keeps increasing at the highest rate among the three samples. After 48 h, the maximum corrosion depth

is about 165 μm in 2.6Cu sample, about twice that in 1Cu sample, and six times that in 0Cu sample. This indicates that IGC susceptibility increases with the increase of Cu content, which is consistent with the results of YUAN et al [25] and DONG et al [26].

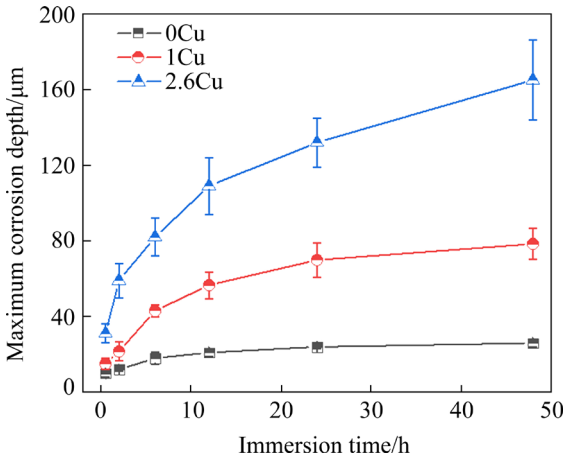

Fig. 7 Maximum corrosion depth of samples after immersion in IGC solution for different time

3.3 Immersion results in EXCO solution

Typical SEM images of samples immersed in the EXCO solution for different time are shown in Fig. 8. Before the immersion, as shown in Figs. 8(a_1, b_1, c_1), the features of Fe-containing particles are the same as that described in Section 3.2. From Figs. 8(a_2, b_2, c_2), after immersion for 3 min, a small number of black pits in the matrix away from Fe-containing particles can be observed in all the samples. This may indicate the corrosion of η phase. After immersion for 10 min, a large number of black pits are formed on the surface of the three samples, but it is difficult to observe intergranular corrosion, as shown in Figs. 8(a_3, b_3, c_3).

After the immersion for 48 h, the surface morphology is shown in Fig. 9. For 0Cu sample, there is the separation of metal, and the surface still retains a metallic luster, and EXCO rating is EA, as shown in Fig. 9(a). From Fig. 9(b), there are a lot of corrosion products on the surface and the loss of metal occurs, and corrosion penetrates into the metal; EXCO rating is EB for 1Cu sample. For 2.6Cu sample, there are a small quantity of corrosion products on the surface, and EXCO may be evaluated to be EA, as shown in Fig. 9(c).

The cross section was examined by OM after immersion for different time to understand the EXCO behavior. As an example, optical micrographs of samples after immersion for 48 h are shown in Fig. 10. In 0Cu sample, a uniform-layering morphology can be seen, and the surface

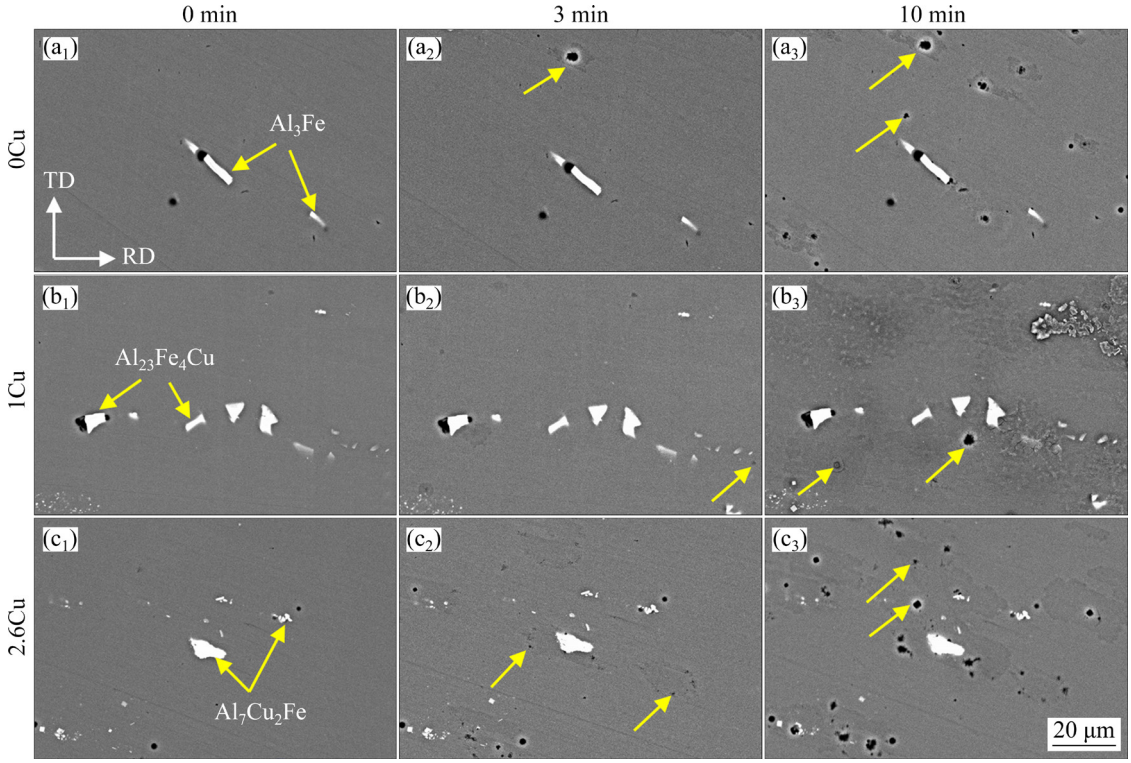

Fig. 8 SEM images of samples before and after immersion in EXCO solution for different time

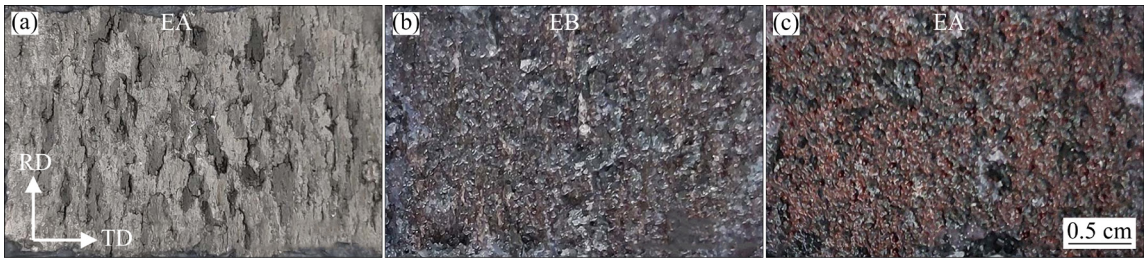

Fig. 9 Digital images showing surface morphology of samples after immersion in EXCO solution for 48 h: (a) 0Cu; (b) 1Cu; (c) 2.6Cu

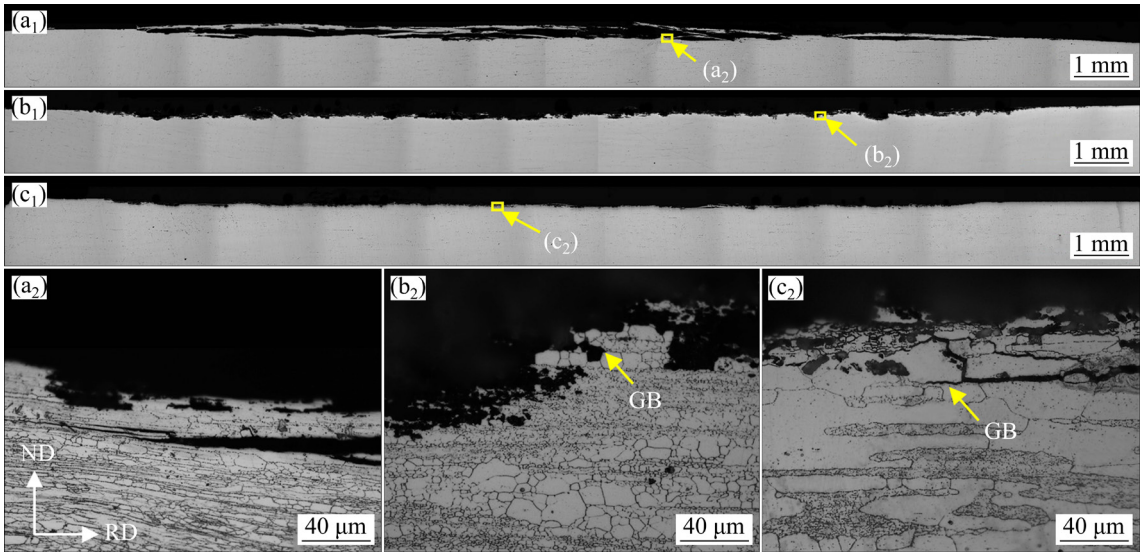

Fig. 10 Optical micrographs of cross section of samples after immersion in EXCO solution for 48 h: (a_1, a_2) 0Cu; (b_1, b_2) 1Cu; (c_1, c_2) 2.6Cu

metal barely falls off, as shown in Fig. 10(a_1). In 1Cu sample, the corrosion exhibits uneven and undulating morphology, and the surface metal completely falls off, as shown in Fig. 10(b_1). In 2.6Cu sample, the surface metal falls off and the corrosion is uniform, as shown in Fig. 10(c_1).

After etching with Graff reagent, the grain structure is revealed, as shown in Figs. 10(a_2, b_2, c_2). The corrosion propagates mainly along GBs for all samples. In 0Cu and 2.6Cu samples, the phenomenon that corrosion tends to propagate along the RD in the cross section can be observed (Figs. 10(a_2, c_2)). However, in 1Cu sample, many corroded grains are exfoliated, and the corrosion propagation does not show obvious directivity on the cross section (Fig. 10(b_2)).

The maximum corrosion depth of samples was measured after immersion for different time, as shown in Fig. 11. After immersion for 1 h, the largest corrosion depth is 38 μm in 2.6Cu sample.

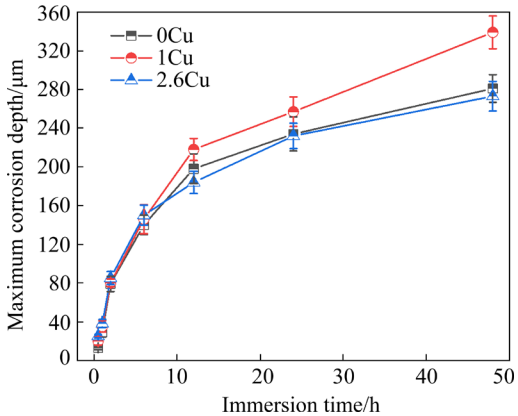

Fig. 11 Maximum corrosion depth of samples after immersion in EXCO solution for different time

The corrosion depth increases with the increase of time, and the increment is similar for the three samples within 6 h. After immersion for 12 h, the corrosion depth is always the largest for 1Cu sample and similar for 0Cu and 1Cu samples. After immersion for 48 h, the maximum depths of EXCO

are about 281, 339 and 273 μm for 0Cu, 1Cu and 2.6Cu samples, respectively, indicating that EXCO susceptibility first increases and then decreases. This phenomenon is different from previous findings by YUAN et al [25], DONG et al [26] and LI et al [24]. The content of Zn and Mg in alloys, the variation range of the Cu content, grain structure and aging treatment in this work are different from those in previous investigations [24−26], and all of these factors can affect the corrosion sensitivity.

3.4 Polarization curves

Polarization curves can be used to evaluate the corrosion resistance of samples in corrosive solutions [17,41]. Figure 12 shows the typical polarization curves of samples immersed in different solutions. All polarization curves exhibit a similar shape, and also similar to those of other Al−Zn−Mg−(Cu) alloys after aging [42]. The polarization curves move towards the positive direction of corrosion potential with the increase of Cu content. Compared with immersion in IGC solution, the polarization curves immersed in EXCO solution tend to move to the negative direction. The corresponding corrosion potential and corrosion current density obtained by Tafel extrapolation method are listed in Table 3.

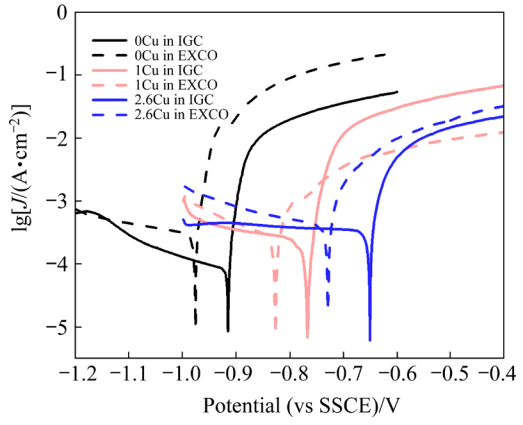

Fig. 12 Polarization curves of samples immersed in IGC and EXCO solutions

It is known that lower corrosion potential means higher corrosion tendency, and higher corrosion current means higher corrosion rate [43]. As Cu content increases, the corrosion potential becomes higher and the corrosion current density becomes larger. The difference in corrosion current density is smaller for the three samples immersed in EXCO solution than in IGC solution. This means that the three samples immersed in IGC solution can show a significant difference in corrosion rate, while there may be smaller difference in corrosion rate in EXCO solution. It is basically consistent with the results in the initial stage of immersion shown in Figs. 7 and 11.

3.5 Surface Volta potential

Scanning Kelvin probe force microscope (SKPFM) is widely used to study the localized corrosion of the aluminum alloys [19,39,44]. Figures 13(a_1−c_1) show the surface Volta potential distribution images of different samples. After tests, according to the indentation mark, OM images of the corresponding regions in Figs. 13(a_1−c_1) are shown in the dotted box in Figs. 13(a_2−c_2), respectively, and GBs can be identified, as shown by the white dotted lines in Figs. 13(a_1−c_1). Typical Volta potential variations along lines across the GB in Figs. 13(a_1−c_1) are shown in Figs. 13(a_3−c_3), respectively. It is seen that the GB regions, which are mainly composed of close-spaced GBPs (Fig. 2), exhibit a lower Volta potential relative to the matrix.

Based on a number of measurements, the Volta potential of the matrix (φ_m) and the Volta potential of GBPs (φ_G), and their differences are listed in Table 4. In alloys with higher Cu content, there is higher Cu content in GBPs (Fig. 3), and thus both φ_m and φ_G increase; however, the increment of φ_m ($\Delta\varphi_m$) is larger than that of φ_G ($\Delta\varphi_G$). This is because the effect of Cu content on the corrosion potential of the matrix is much larger than that on GBPs, which is verified in previous investigations.

Table 3 Electrochemical parameters obtained from Tafel slope analysis in Fig. 12

Sample	In IGC solution		In EXCO solution	
	φ_{corr} (vs SSCE)/V	J_{corr}/(μA·cm^{-2})	φ_{corr} (vs SSCE)/V	J_{corr}/(μA·cm^{-2})
0Cu	−0.915±0.007	70.8±4.5	−0.976±0.004	275.5±21.2
1Cu	−0.767±0.013	108.1±12.6	−0.824±0.009	318.8±27.7
2.6Cu	−0.651±0.011	339.4±15.1	−0.728±0.010	369.1±19.4

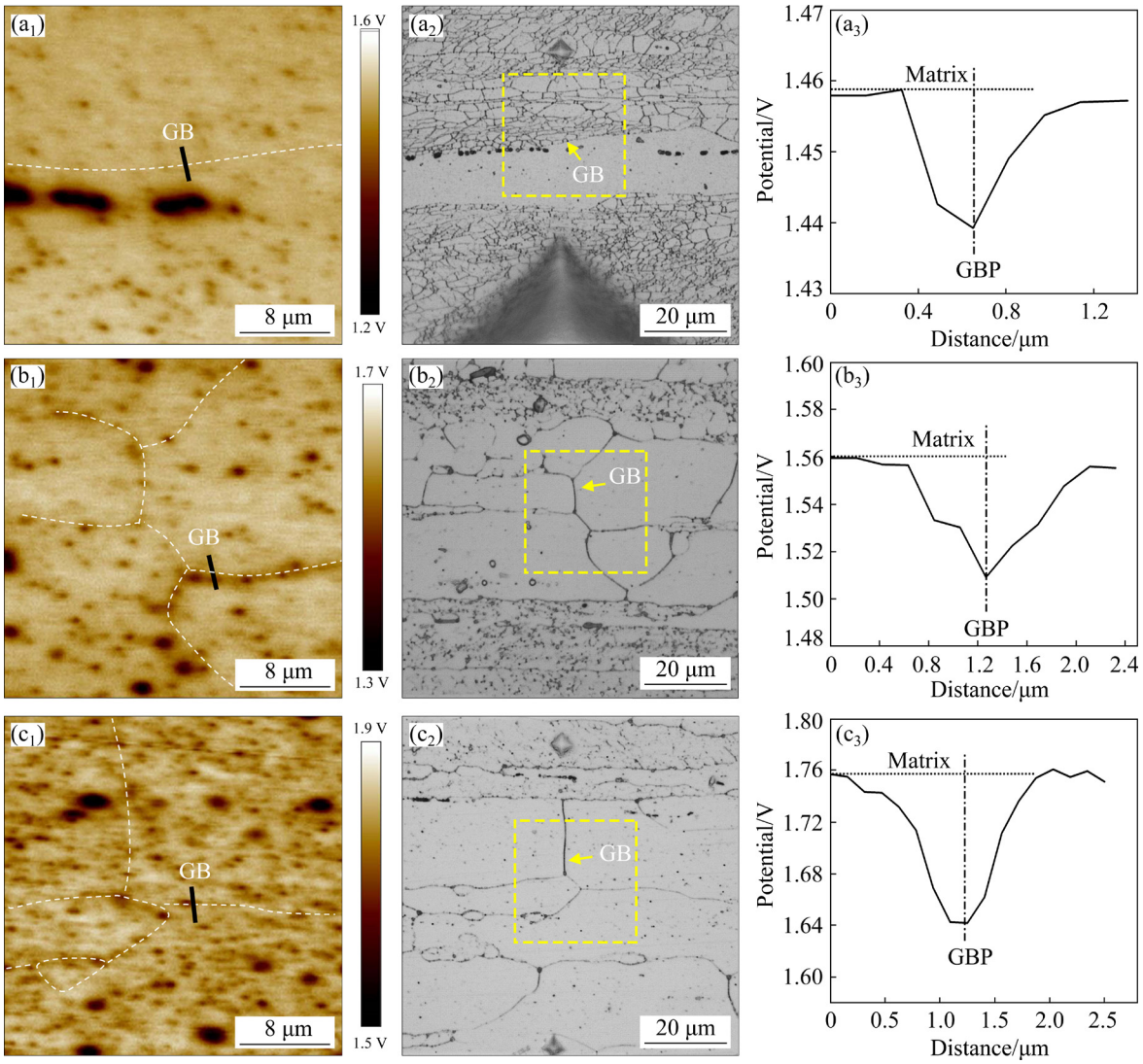

Fig. 13 Volta potential distribution (a_1−c_1), OM images etched with Graff reagent (a_2−c_2), and Volta potential variation (a_3−c_3) along lines in (a_1−c_1): (a_1−a_3) 0Cu; (b_1−b_3) 1Cu; (c_1−c_3) 2.6Cu

Table 4 Volta potential of matrix and GBPs and their differences

Sample	φ_m/mV	$\Delta\varphi_m$/mV	φ_G/mV	$\Delta\varphi_G$/mV	$(\varphi_m-\varphi_G)$/mV
0Cu	1459.2±19.4	−	1430.0±10.2	−	29.2±8.2
1Cu	1558.7±25.1	99.5	1509.3±16.3	79.3	49.4±9.8
2.6Cu	1751.1±27.9	290.9	1677.9±21.7	247.9	80.0±13.1

It was found that when Cu content increases from 0.01 to 0.89 at.%, the corrosion potential of the matrix increases by 252 mV while the corrosion potential of η phase hardly increases [17,41]. As a result, the Volta potential difference between GBPs and the matrix (VDPGM, $\varphi_m-\varphi_G$) gradually increases with the increase of Cu content, making GBPs more susceptible to corrosion. It is contrary to the result that GBPs with a higher Cu content are more noble [21,26]. This is because in these studies only the effect of Cu content on the potential of GBPs was considered, but the fact that the increase of Cu content can increase the potential of the matrix was ignored.

4 Discussion

EXCO is generally considered to be a

special form of IGC, and the materials with high IGC susceptibility often exhibit high EXCO susceptibility [12,25,45,46]. However, in this work, it is found that as Cu content increases, IGC susceptibility increases, while EXCO susceptibility first increases and then decreases; 1Cu sample exhibits slight IGC but severe EXCO. The initiation and propagation of corrosion must be considered simultaneously.

4.1 Corrosion initiation

In previous investigations [24−27], little attention was paid to the effect of Cu on corrosion initiation. Corrosion initiation of GBPs is closely related to the VDPGM. There are only pits in 0Cu sample, and IGC becomes significant with the increase of Cu content (Fig. 6). This means that the critical Volta potential difference for triggering corrosion of GBPs in IGC solution is close to the VDPGM of 1Cu sample, about 49.4 mV (Table 4). Similarly, GBs of the three sample are corroded after immersion in EXCO solution (Fig. 10), so the critical Volta potential difference for triggering corrosion of GBPs in EXCO solution is less than 29.2 mV.

In the initiation stage, EXCO and IGC show different behavior. In IGC solution, the VDPGM of 0Cu sample does not exceed the critical value, so the corrosion of GBPs is not triggered. The VDPGM of 1Cu sample is similar to the critical value, while the VDPGM of 2.6Cu sample is higher than the critical value. Therefore, more GBPs are corroded in 2.6Cu sample, forming more black pits after immersion for 10 min (Fig. 4). After immersion in EXCO solution, the VDPGM of all samples is higher than the critical value. η phase at GBs is attacked, and after immersion for 3 min, corrosion pits can be observed in the three samples (Fig. 8).

4.2 Corrosion propagation

It is known that the features of GBPs and PFZ are important factors that affect the propagation of IGC and EXCO [47,48]. In the three samples, the GBPs with a slight difference in their sizes are closely-spaced, and the width of PFZ is similar (Fig. 2). This indicates that the features of GBPs and PFZ are not the main factors leading to the difference in IGC and EXCO susceptibility of the three samples.

Corrosion initiation can affect corrosion propagation. After immersion in IGC solution, GBPs of 0Cu sample are not corroded, and the IGC does not initiate and thus does not propagate. The propagation rate of pitting corrosion is much lower than that of IGC, so the corrosion depth of 0Cu sample is very small (Fig. 7). With the increase of Cu content, GBPs is more susceptible to corrosion, and thus corrosion can propagate more rapidly along GBs. As a result, the sample with a higher Cu content exhibits a higher IGC susceptibility.

Unlike the immersion in IGC solution, the corrosion of GBPs is triggered when the three samples are immersed in EXCO solution. After the dissolution of GBPs, a large amounts of corrosion products are produced. The accumulation of corrosion products creates wedging stress at GBs, causes large surface strain, and finally results in blistered or exfoliated morphology [49,50].

The grain structure can affect the exfoliation of the metal [49,51], which in turn affects the propagation of EXCO. It is thought that blisters form more readily in material with higher aspect ratio grains, but the strain accumulation is slow. However, in material with lower aspect ratio grains, the strain in the surface increases more rapidly until it exceeds the fracture strain [49,52]. This indicates that the surface grains with lower aspect ratio are more likely to fall off. After the surface grains fall off, a new surface is exposed to the corrosive solution, and the corrosion can continue to propagate rapidly. However, if the metal surface does not fall off, it is difficult for corrosive solution to enter the corrosion tip, and the corrosion propagation is hindered. The aspect ratio of grains shows a trend of 0Cu>2.6Cu>1Cu (Table 2), so the surface metal is easy to fall off and corrosion can penetrate to a large depth in 1Cu sample (Fig. 10).

The grain structure can also affect the direction of corrosion propagation [53], which in turn affects the depth of EXCO. The corrosion path in three samples is shown schematically in Fig. 14. It is known that SGBs can contribute to higher resistance to corrosion than GBs [54,55]. The recrystallized grains of 0Cu and 2.6Cu samples are distributed in layers along the ND (Fig. 1). When corrosion propagates along the ND, it can be hindered by SGBs (Fig. 14(a)). As a result, a small corrosion depth can be observed. For 1Cu sample, the length of GBs is the largest (Table 2). Thus, the

number of GBPs is the largest and it is not conducive to EXCO resistance [13]. The small and equiaxed-shape recrystallized grains result in corrosion that can easily propagates along the ND (Fig. 14(b)), and as a result, a large corrosion depth is formed.

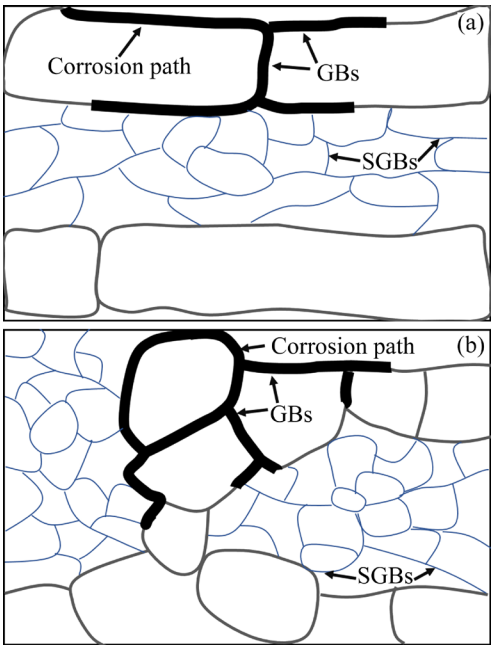

Fig. 14 Schematic diagrams of propagation of EXCO in different samples: (a) 0Cu and 2.6Cu samples; (b) 1Cu sample

5 Conclusions

(1) With Cu content increasing from 0 to 2.6 wt.%, IGC susceptibility increases, while EXCO susceptibility first increases and then decreases, reaching the maximum at Cu content of 1 wt.%.

(2) The initiation and propagation of IGC are mainly related to the potential difference between GBPs and the matrix. As Cu content increases, the potential difference between GBPs and the matrix increases, and thus IGC susceptibility increases.

(3) Cu content has a little effect on the initiation of EXCO. Cu changes the grain structure, and therefore leads to the differences in the propagation of EXCO for different samples. For 1Cu sample, the small and equiaxed-shape grains are more likely to fall off and make the corrosion more likely to penetrate along the depth direction. As a result, EXCO susceptibility is the highest in 1Cu sample.

References

[1] STARKE E A, STALEYT J T. Application of modern aluminum alloys to aircraft [J]. Progress in Aerospace Sciences, 1996, 32: 131−172.

[2] ROMETSCH P A, ZHANG Y, KNIGHT S. Heat treatment of 7xxx series aluminium alloys−some recent developments [J]. Transactions of Nonferrous Metals Society of China, 2014, 24(7): 2003−2017.

[3] MA Zhi-min, ZHANG Yong, LIU Sheng-dan, DENG Yun-lai, ZHANG Xin-ming. Quenching sensitivity and heterogeneous precipitation behavior of AA7136 alloy [J]. Transactions of Nonferrous Metals Society of China, 2021, 31(11): 3356−3369.

[4] HE Ke-zhun, LI Qun, LIU Sheng-dan, ZHANG Xin-ming, ZHOU Ke-chao. Influence of pre-stretching on quench sensitive effect of high-strength Al−Zn−Mg−Cu−Zr alloy sheet [J]. Journal of Central South University, 2021, 28(9): 2660−2669.

[5] CHEN Song-yi, CHEN Kang-hua, PENG Guo-sheng, LIANG Xin, CHEN Xue-hai. Effect of quenching rate on microstructure and stress corrosion cracking of 7085 aluminum alloy [J]. Transactions of Nonferrous Metals Society of China, 2012, 22(1): 47−52.

[6] KAIRY S K, TURK S, BIRBILIS N, SHEKHTER A. The role of microstructure and microchemistry on intergranular corrosion of aluminium alloy AA7085-T7452 [J]. Corrosion Science, 2018, 143: 414−427.

[7] LI J F, ZHENG Z Q, LI S C, CHEN W J, REN W D, ZHAO X S. Simulation study on function mechanism of some precipitates in localized corrosion of Al alloys [J]. Corrosion Science, 2007, 49: 2436−2449.

[8] BIRBILIS N, BUCHHEIT R G. Electrochemical characteristics of intermetallic phases in aluminum alloys [J]. Journal of the Electrochemical Society, 2005, 152(4): B140−B151.

[9] CHUBB J P, MORAD T A, HOCKENHULL B S, BRISTOW J W. The effect of exfoliation corrosion on the fracture and fatigue behaviour of 7178-T6 aluminium [J]. International Journal of Fatigue, 1995, 17(1): 49−54.

[10] KIM S, BURNS J T, GANGLOFF R P. Fatigue crack formation and growth from localized corrosion in Al−Zn−Mg−Cu [J]. Engineering Fracture Mechanics, 2009, 76(5): 651−667.

[11] FANG H C, LUO F H, CHEN K H. Effect of intermetallic phases and recrystallization on the corrosion and fracture behavior of an Al−Zn−Mg−Cu−Zr−Yb−Cr alloy [J]. Materials Science and Engineering A, 2017, 684: 480−490.

[12] MARLAUD T, MALKI B, HENON C, DESCHAMPS A, BAROUX B. Relationship between alloy composition, microstructure and exfoliation corrosion in Al−Zn−Mg−Cu alloys [J]. Corrosion Science, 2011, 53: 3139−3149.

[13] LIU S D, CHEN B, LI C B, DAI Y, DENG Y L, ZHANG X M. Mechanism of low exfoliation corrosion resistance due to slow quenching in high strength aluminium alloy [J]. Corrosion Science, 2015, 91: 203−212.

[14] CHEN Ming-yang, XU Zheng, HE Ke-zhun, LIU Sheng-dan,

ZHANG Yong. Local corrosion mechanism of an Al−Zn−Mg−Cu alloy in oxygenated chloride solution: Cathode activity of quenching-induced η precipitates [J]. Corrosion Science, 2021, 191: 109743.

[15] XIAO Yan-ping, PAN Qing-lin, LI Wen-bin, LIU Xiao-yan, HE Yun-bin. Influence of retrogression and re-aging treatment on corrosion behaviour of an Al−Zn−Mg−Cu alloy [J]. Materials & Design, 2011, 32: 2149−2156.

[16] DESCHAMPS A, BRÉCHET Y, LIVET F. Influence of copper addition on precipitation kinetics and hardening in Al−Zn−Mg alloy [J]. Materials Science and Technology, 1999, 15: 993−1000.

[17] MENG Q, FRANKEL G S. Effect of Cu content on corrosion behavior of 7xxx series aluminum alloys [J]. Journal of the Electrochemical Society, 2004, 151(5): B271−B283.

[18] VARGEL C. Corrosion of aluminium [M]. Second Edition. Amsterdam: Elsevier, 2019.

[19] SONG Feng-xuan, ZHANG Xin-ming, LIU Sheng-dan, TAN Qi, LI Dong-feng. The effect of quench rate and overageing temper on the corrosion behaviour of AA7050 [J]. Corrosion Science, 2014, 78: 276−286.

[20] RAMGOPAL T, GOUMA P I, FRANKEL G S. Role of grain-boundary precipitates and solute-depleted zone on the intergranular corrosion of aluminum alloy 7150 [J]. Corrosion, 2002, 58(8): 687−697.

[21] SARKAR B, MAREK M, STARKE JR E A. The effect of copper content and heat treatment on the stress corrosion characteristics of Al−6Zn−2Mg−XCu alloys [J]. Metallurgical Transactions A, 1981, 12: 1939−1943.

[22] KNIGHT S P, POHL K, HOLROYD N J H, BIRBILIS N, ROMETSCH P A, MUDDEL B C, GOSWAMI R, LYNCH S P. Some effects of alloy composition on stress corrosion cracking in Al−Zn−Mg−Cu alloys [J]. Corrosion Science, 2015, 98: 50−62.

[23] KNIGHT S P, BIRBILIS N, MUDDEL B C, TUREMAN A R, LYNCH S P. Correlations between intergranular stress corrosion cracking, grain-boundary microchemistry, and grain-boundary electrochemistry for Al−Zn−Mg−Cu alloys [J]. Corrosion Science, 2010, 52: 4073−4080.

[24] LI Yan-xi, CHEN Kang-hua, HUANG Lan-ping, XU Cheng-fu, CHEN Song-yi. Effect of copper content on microstructure and properties of super-high strength Al−Zn−Mg−Cu−Zr−Cr−Yb alloy [J]. Materials Science and Engineering of Powder Metallurgy, 2014, 19(5): 727−735. (in Chinese)

[25] YUAN Ding-ling, CHEN Kang-hua, CHEN Song-yi, ZHOU Liang, CHANG Jiang-yu, HUANG Lan-ping, YI You-ping. Enhancing stress corrosion cracking resistance of low Cu-containing Al−Zn−Mg−Cu alloys by slow quench rate [J]. Materials & Design, 2019, 164: 107558.

[26] DONG Peng-xuan, CHEN Song-yi, CHEN Kang-hua. Effects of Cu content on microstructure and properties of super-high-strength Al−9.3Zn−2.4Mg−xCu−Zr alloy [J]. Journal of Alloys and Compounds, 2019, 788: 329−337.

[27] LIU Li, JIA Ying-ying, JIANG Jian-tang, ZHANG Bo, LI Guo-ai, SHAO Wen-zhu, ZHEN Liang. The effect of Cu and Sc on the localized corrosion resistance of Al−Zn−Mg−X alloys [J]. Journal of Alloys and Compounds, 2019, 799: 1−14.

[28] GB/T 7998—2005. Test method for intergranular corrosion of aluminium alloy [S]. (in Chinese)

[29] GB/T 22639—2008. Test method of exfoliation corrosion for wrought aluminium and aluminium alloys [S]. (in Chinese)

[30] LIU Jing, YAO Pei, ZHAO Nai-qin, SHI Chun-sheng, LI Hui-jun, LI Xuan, XI De-sheng, YANG Shuo. Effect of minor Sc and Zr on recrystallization behavior and mechanical properties of novel Al−Zn−Mg−Cu alloys [J]. Journal of Alloys and Compounds, 2016, 657: 717−725.

[31] ADAM K F, LONG Z, FIELD D P. Analysis of particle-stimulated nucleation (PSN)-dominated recrystallization for hot-rolled 7050 aluminum alloy [J]. Metallurgical and Materials Transactions A, 2017, 48: 2062−2076.

[32] UMPHREYS F J, HATHERLY M. Recrystallization and related annealing phenomena [M]. 2nd ed. Amsterdam: Elsevier, 2004.

[33] SONG Feng-xuan, ZHANG Xin-ming, LIU Sheng-dan, TAN Qi, LI Dong-feng. Exfoliation corrosion behavior of 7050-T6 aluminum alloy treated with various quench transfer time [J]. Transactions of Nonferrous Metals Society of China, 2014, 24(7): 2258−2265.

[34] MARLAUD T, DESCHAMPS A, BLEY F, LEFEBVRE W, BAROUX B. Influence of alloy composition and heat treatment on precipitate composition in Al−Zn−Mg−Cu alloys [J]. Acta Materialia, 2010, 58: 248−260.

[35] HE Xiao-ning, LI Shao-yin, CAO Guo-qin, HU Jun-hua, ZHANG Jin-hua, QIAO Rui, PAN Jin-min, SHAO Guo-sheng. In situ atomic-scale engineering of the chemistry and structure of the grain boundaries region of $Li_{3x}La_{2/3-x}TiO_3$ [J]. Scripta Materialia, 2020, 185: 134−139.

[36] WANG Shan-shan, HUANG I-wen, YANG Li, JIANG Jian-tang, Chen Jun-feng, DAI Sheng-long, SEIDMAN D N, FRANKEL G S, ZHEN Liang. Effect of Cu content and aging conditions on pitting corrosion damage of 7xxx series aluminum alloys [J]. Journal of the Electrochemical Society, 2015, 162(4): C150−C160.

[37] GAO M, FENG C R, WEI R P. An analytical electron microscopy study of constituent particles in commercial 7075-T6 and 2024-T3 alloys [J]. Metallurgical and Materials Transactions A, 1998, 29: 1145−1151.

[38] SINGH S S, SCHWARTZSTEIN C, WILLIAMS J J, XIAO X, CARLO F D, CHAWLA N. 3D microstructural characterization and mechanical properties of constituent particles in Al 7075 alloys using X-ray synchrotron tomography and nanoindentation [J]. Journal of Alloys and Compounds, 2014, 602: 163−174.

[39] SUN Yuan-wei, PAN Qing-lin, SUN Yu-qiao, WANG Wei-yi, HUANG Zhi-qi, WANG Xiang-dong, HU Quan, Localized corrosion behavior associated with Al_7Cu_2Fe intermetallic in Al−Zn−Mg−Cu−Zr alloy [J]. Journal of Alloys and Compounds, 2019, 783: 329−340.

[40] NIVERTY S, KALE C, SOLANKI K N, CHAWLA N. Multiscale investigation of corrosion damage initiation and propagation in AA7075-T651 alloy using correlative microscopy [J]. Corrosion Science, 2021, 185: 109429.

[41] RAMGOPAL T, SCHMUTZ P, FRANKEL G S. Electrochemical behavior of thin film analogs of Mg (Zn, Cu, Al)$_2$ [J]. Journal of the Electrochemical Society, 2001, 148(9):

B348−B356.
[42] LIU S D, WANG Q, YANG Z S, CHAI W R, CHEN J C, YE L Y, TANG J G. Effect of minor Ge addition on microstructure and localized corrosion behavior of Al−Zn−Mg alloy sheet [J]. Materials Characterization, 2019, 156: 109837.
[43] ZUO Jin-rong, HOU Long-gang, SHI Jin-tao, CUI Hua, ZHUANG Lin-zhong, ZHANG Ji-shan. Enhanced plasticity and corrosion resistance of high strength Al−Zn−Mg−Cu alloy processed by an improved thermomechanical processing [J]. Journal of Alloys and Compounds, 2017, 716: 220−230.
[44] MA Zhi-min, LIU Jia, YANG Zhen-shen, LIU Sheng-dan, ZHANG Yong. Effect of cooling rate and grain structure on the exfoliation corrosion susceptibility of AA 7136 alloy [J]. Materials Characterization, 2020, 168: 110533.
[45] LU Xiang-han, HAN Xiao-lei., DU Zhi-wei, WANG Guo-jun, LU Li-ying, LEI Jin-qin, ZHOU Tie-tao. Effect of microstructure on exfoliation corrosion resistance in an Al−Zn−Mg alloy [J]. Materials Characterization, 2018, 135: 167−174.
[46] TANG Zhong-qin, JIANG FENG., LONG Meng-jun, JIANG Jing-yu., LIU Hui-fang, TONG Meng-meng. Effect of annealing temperature on microstructure, mechanical properties and corrosion behavior of Al−Mg−Mn−Sc−Zr alloy [J]. Applied Surface Science, 2020, 514: 146081.
[47] HUANG Lan-ping, CHEN Kang-hua, LI Song. Influence of grain-boundary pre-precipitation and corrosion characteristics of inter-granular phases on corrosion behaviors of an Al−Zn−Mg−Cu alloy [J]. Materials Science and Engineering B, 2012, 177: 862−868.
[48] LI Dong-feng, YIN Bang-wen, LEI Yue, LIU Sheng-dan, DENG Yun-lai, ZHANG Xin-ming. Critical quenching rate for high hardness and good exfoliation corrosion resistance of Al−Zn−Mg−Cu alloy plate [J]. Metals and Materials International, 2016, 22(2): 222−228.
[49] ROBINSON M J. Mathematical modelling of exfoliation corrosion in high strength aluminium alloys [J]. Corrosion Science, 1982, 22: 775−790.
[50] MCNAUGHTAN D, WORSFOLD M, ROBINSON M J. Corrosion product force measurements in the study of exfoliation and stress corrosion cracking in high strength aluminium alloys [J]. Corrosion Science, 2003, 45: 2377−2389.
[51] ZHAO X, FRANKEL G S. Quantitative study of exfoliation corrosion: Exfoliation of slices in humidity technique [J]. Corrosion Science, 2007, 49: 920−938.
[52] WLOKA J, HACK T, VIRTANEN S. Influence of temper and surface condition on the exfoliation behaviour of high strength Al−Zn−Mg−Cu alloys [J]. Corrosion Science, 2007, 49: 1437−1449.
[53] MA Zhi-min, LIU Jia, LIU Sheng-dan, ZHANG Yong, DENG Yun-lai. Quench-induced contributions of high angle grain boundary and low angle grain boundary to exfoliation corrosion propagation in an AlZnMgCu alloy [J]. Journal of Materials Research and Technology, 2021, 15: 6866−6870.
[54] FANG H C, CHAO H, CHEN K H. Effect of recrystallization on intergranular fracture and corrosion of Al−Zn−Mg−Cu−Zr alloy [J]. Journal of Alloys and Compounds, 2015, 622:166−173.
[55] FANG H C, CHAO H, CHEN K H. Effect of Zr, Er and Cr additions on microstructures and properties of Al−Zn−Mg−Cu alloys [J]. Materials Science and Engineering A, 2014, 610: 10−16.

铜含量对 Al−Zn−Mg−(Cu)合金晶间腐蚀和剥落腐蚀敏感性的影响

张梦晗[1,2]，刘胜胆[1,2,3]，蒋靖宇[4]，韦卫昌[1,2]

1. 中南大学 材料科学与工程学院，长沙 410083；
2. 中南大学 有色金属材料科学与工程教育部重点实验室，长沙 410083；
3. 中南大学 轻质高强结构材料重点实验室，长沙 410083；
4. 中南大学 冶金与环境学院，长沙 410083

摘 要：通过电化学试验和浸泡试验，使用电子背散射衍射、光学显微镜、扫描电镜和扫描透射电镜及扫描开尔文探针原子力显微镜，研究铜含量对 Al−Zn−Mg−(Cu)合金晶间腐蚀和剥落腐蚀敏感性的影响。结果表明，铜含量从 0 增加至 2.6%(质量分数)，晶间腐蚀敏感性增高；而剥落腐蚀敏感性先增高后降低，铜含量为 1%时的剥落腐蚀敏感性最高。随着 Cu 含量的增加，再结晶分数增加，再结晶晶粒的长宽比先减小后增大；晶界析出相与基体的伏打电势差提高，使晶界析出相更易被腐蚀。根据晶界析出相的形貌特征、晶粒组织和晶界析出相与基体的伏打电势差，对晶间腐蚀和剥落腐蚀的萌生和扩展进行讨论。

关键词：铜；晶间腐蚀；剥落腐蚀；Al−Zn−Mg−Cu 合金；扫描开尔文探针原子力显微镜

(Edited by Bing YANG)